AIP Advances

RESEARCH ARTICLE | JUNE 21 2023

Atomistic model of the anisotropic response of *ortho*-Mo_2C to indentation

Ingrid M. Padilla Espinosa ; Yenal Karaaslan ; Cem Sevik ; Ashlie Martini

Check for updates

AIP Advances 13, 065125 (2023)
https://doi.org/10.1063/5.0150030

CrossMark

View Online

Export Citation

Articles You May Be Interested In

Superconductivity of monolayer Mo_2C: The key role of functional groups

J. Chem. Phys. (January 2017)

In-Cu alloy substrates for low-temperature chemical vapor deposition of Mo_2C

Journal of Vacuum Science & Technology A (December 2020)

Li-adsorption on doped Mo_2C monolayer: A novel electrode material for Li-ion batteries

AIP Conference Proceedings (April 2018)

31 August 2023 09:13:32

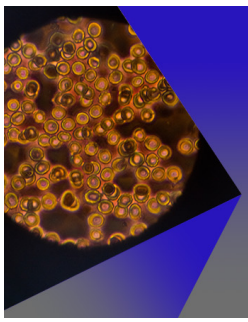

AIP Advances
Special Topic: Medical Applications of Nanoscience and Nanotechnology
Submit Today!
AIP Publishing

AIP Publishing

Atomistic model of the anisotropic response of *ortho*-Mo_2C to indentation

Cite as: AIP Advances 13, 065125 (2023); doi: 10.1063/5.0150030
Submitted: 12 March 2023 • Accepted: 5 June 2023 •
Published Online: 21 June 2023

View Online Export Citation CrossMark

Ingrid M. Padilla Espinosa,[1] Yenal Karaaslan,[2] Cem Sevik,[3,4] and Ashlie Martini[1,a)]

AFFILIATIONS

[1] Department of Mechanical Engineering, University of California, Merced, Merced, California 95340, USA
[2] Department of Fundamental Sciences, Air NCO Vocational HE School, Turkish National Defence University, 35415 İzmir, Türkiye
[3] Department of Mechanical Engineering, Eskişehir Technical University, 26555 Eskişehir, Türkiye
[4] Department of Physics-NANOlab Center of Excellence, University of Antwerp, Groenenborgerlaan 171, B-2020 Antwerp, Belgium

[a)] **Author to whom correspondence should be addressed:** amartini@ucmerced.edu

ABSTRACT

Molybdenum carbide has various applications for which studying the material using classical molecular dynamics simulations would be valuable. Here, we develop an empirical potential within the Tersoff formalism using particle swarm optimization for the orthorhombic phase of Mo_2C. The developed potential is shown to predict lattice constants, elastic properties, and equation of state results that are consistent with current and previously reported results from experiments and first principles calculations. We demonstrate the potential with simulations of indentation using multiple indenter sizes that load and unload in three different directions relative to the crystallographic lattice of orthorhombic Mo_2C. Direction-dependent force-displacement trends are analyzed and explained in terms of the spatial distributions of stress and strain within the material during indentation. This study reveals the anisotropic elasticity of orthorhombic Mo_2C and, more generally, provides researchers with a new empirical potential that can be used to explore the properties and behavior of the material going forward.

© 2023 Author(s). All article content, except where otherwise noted, is licensed under a Creative Commons Attribution (CC BY) license (http://creativecommons.org/licenses/by/4.0/). https://doi.org/10.1063/5.0150030

31 August 2023 09:13:32

Molybdenum carbide is a transition metal carbide with high melting temperature and hardness, good thermal and mechanical stability, and excellent corrosion resistance. These properties make the material ideal for applications such as wear-resistant coatings.[1] It also is a promising material for catalysis, particularly hydrogen evolution reactions, for which it is both cheaper and more readily available than the typical noble metals.[2] There are multiple crystallographic phases of molybdenum carbide, but here we focus on the orthogonal phase, which has been reported to be more stable than the hexagonal phases.[3] In many applications, *ortho*-Mo_2C is the functional component of coatings, so the mechanical properties of the near-surface material are important. One way to characterize the mechanical properties and investigate the deformation mechanisms of a material, particularly near surfaces, is using indentation techniques.[4] These techniques also enable directional mechanical testing and can be used to characterize the anisotropic properties.[5,6] However, relationships between the atomic structure and the measured properties cannot be explained by indentation experiments alone. Molecular dynamics (MD) simulations have been used to provide insight into the direction-dependent response to indentation of various materials, including metals,[6] polymers,[7] semiconductors,[8] and nanomaterials.[9] However, this approach requires the availability of an interatomic potential, or force field, for the material of interest.

Many different formalisms can be used to describe interaction energies in terms of atomic spatial coordinates.[10] For molybdenum carbide, the universal force field (UFF)[11] has been used to study the absorption of CO. However, accurate modeling of indentation and mechanical properties usually requires parameterization tailored to characterize the properties of interest.[12] From the different formalisms available, optimized Tersoff potentials have previously demonstrated high accuracy in describing the mechanical properties of various materials, for example, Fe–C systems,[13] silicon carbide,[14] boron nitride,[15] and graphene.[16]

Here, we developed an empirical Tersoff potential for *ortho*-Mo_2C based on density functional theory (DFT) energies. The elastic mechanical properties of *ortho*-Mo_2C predicted by the new potential were compared to the results from DFT and previously

© Author(s) 2023

reported experiments. Then, the potential was used to simulate indentation on three different *ortho*-Mo_2C surface facets with variable sized nanoscale indenters. The resulting force vs displacement trends showed surface facet anisotropy, which was then explained in terms of the atomic distributions of stress and strain in the material during indentation.

The orthorhombic phase has been previously denoted α-Mo_2C[17,18] but, following the notation convention defined by the Joint Committee on Power Diffraction Standards' data files and based on its ζ-Fe_2N-like structure, this phase was later denoted β-Mo_2C.[19] Here, we call the phase *ortho*-Mo_2C, following a recent example.[20] A summary of lattice parameters and nomenclatures used for orthorhombic Mo_2C is given in Sec. S1 of the supplementary material. The *ortho*-Mo_2C (a < b < c) simulated structure is shown in Fig. 1(a).

We developed a set of parameters with the formalism of the Tersoff empirical interatomic potential (EIAP), see Sec. S2. In this study, the particle swarm optimization (PSO) method[23–25] was used to obtain two one-body terms, n and β, for Mo and C atoms, four two-body terms, A, B, λ_1, and λ_2, for Mo–C (or C–Mo) interactions, and four three-body terms λ_3, c, d, and h, for Mo–C–C (and C–Mo–Mo). The fitness function for PSO that correlates with the calculated parameters with the desired physical characteristics is defined as

$$f(n^{Mo}, \beta^{Mo}, n^{C}, \beta^{C}, A, B, \lambda_1, \lambda_2, \lambda_3^{Mo}, c^{Mo}, d^{Mo}, h^{Mo}, \lambda_3^{C}, c^{C}, d^{C}, h^{C}) = \sum_{l=1}^{L} \left(\frac{|d_l - a_l|}{d_l} \right), \quad (1)$$

where d_l denotes the desired value of the characteristic l obtained by DFT (first-principles calculations), a_l denotes the actual value of the characteristic l obtained via a given Tersoff potential parameter set, and L is the total number of certain physical characteristics of the Mo_2C crystal structure to be optimized simultaneously. Here, the lattice constants and equation of states (EOS) defined as the deviation from the equilibrium energy via isotropic tensile and compressive strain, stiffness constants, bulk and shear moduli are considered. The values are determined by using the General Utility Lattice Program (GULP) code[26] throughout the EIAP parameter set optimization process. The Tersoff potential parameters optimized for *ortho*-Mo_2C are given in Table I.

To calculate the desired values of the variables, in the first-principles calculations, we use the pseudopotential plane-wave method based on DFT within the Perdew–Burke–Ernzerhof (PBE) formulation by means of the Vienna *Ab initio* Simulation Package (VASP).[27–31] A plane-wave basis set with an energy cut-off of 700 eV and a mesh of 12 × 12 × 12 k-point grids centered at Γ within the Monkhorst–Pack scheme in the Brillouin zone are used. Once the atomic positions and cell parameters of the Mo_2C unit cell are relaxed, we obtain the cell parameters as a = 4.7387 Å, b = 5.2331 Å, and c = 6.0601 Å for an external pressure of 0.00 kbar. To obtain the phonon dispersion, the phonopy[32] code is employed by using the force constants computed from the density-functional perturbation theory.[33] Phonon dispersion results, although not the focus of this study, are provided in Fig. 1(b). The calculation is carried out with a 2 × 2 × 2 conventional supercell structure, considering Γ centered 6 × 6 × 6 k-point grids for Brillouin-zone sampling. Obtaining the phonon dispersion with the lowest deviation rates by means of the

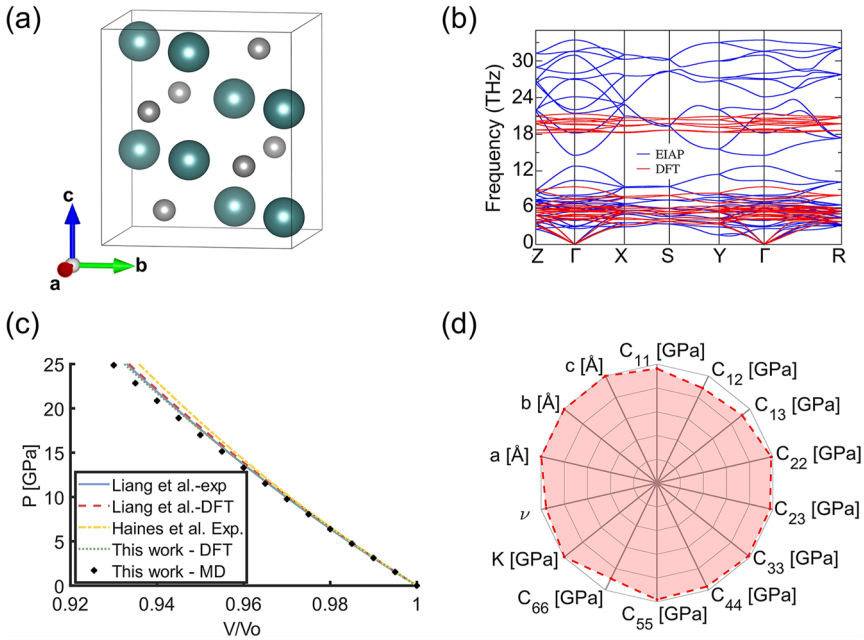

FIG. 1. (a) Atomic structure of *ortho*-Mo_2C. (b) Spinel phonon dispersion from DFT calculations. (c) Compressibility of the normalized unit cell volumes fitted to the third-order Birch–Murnaghan equation of state (EOS) for *ortho*-Mo_2C. Blue solid line: experimental calculations with ultrasonic elastic wave interferometry;[21] red dashed line: DFT calculations;[21] yellow dashed-dotted line: experimental calculations with x-ray diffraction in a diamond anvil;[22] green dotted line: DFT calculations; black asterisks: MD simulations. (d) Radar plots summarizing the accuracy of MD calculations based on comparisons to experimental values and DFT calculations.

31 August 2023 09:13:32

© Author(s) 2023

TABLE I. Optimized Tersoff-type EIAP parameters obtained for *ortho*-Mo_2C.

EIAP parameters	Mo (Mo–C and Mo–C–C)	C (C–Mo and C–Mo–Mo)
n	0.844 0	1.123 0
β	$36.837\,2 \times 10^{-6}$	$30.922\,0 \times 10^{-6}$
A (eV)	7 041.471 4	7 041.471 4
B (eV)	2 694.029 1	2 694.029 1
λ_1 (Å^{-1})	2.943 3	2.943 3
λ_2 (Å^{-1})	2.317 1	2.317 1
λ_3 (Å^{-1})	4.397 8	2.167 0
c	53 270.797 8	112 790.042 8
d	28.203 1	28.478 0
h	−0.916 6	−0.241 0
R (Å)	2.75	2.75
D (Å)	0.15	0.15

TABLE II. Summary of the lattice parameters and elastic properties for the orthorhombic Mo_2C phase calculated using molecular dynamics with the developed Tersoff potential and density functional theory.

	MD	DFT
C_{11} (GPa)	444.311	464.952
C_{12} (GPa)	205.543	234.814
C_{13} (GPa)	252.702	225.983
C_{22} (GPa)	510.200	501.418
C_{23} (GPa)	171.444	176.644
C_{33} (GPa)	508.717	499.027
C_{44} (GPa)	178.735	171.253
C_{55} (GPa)	146.453	142.965
C_{66} (GPa)	217.261	188.121
K (GPa)	305.586	304.410
v	0.301	0.284
a (Å)	4.733	4.739
b (Å)	5.214	5.233
c (Å)	6.058	6.060

developed empirical potentials is especially important for the accurate estimation of the lattice thermal conductivity of the materials.[23] In this respect, two alternative Tersoff-type EIAP parameter sets, which give more consistent phonon dispersion curves and thus are believed to allow a more accurate estimation of the thermal properties of the *ortho*-Mo_2C, are presented in Sec. S3 of the supplementary material.

Simulations of the structural and mechanical properties of *ortho*-Mo_2C with the developed set of Tersoff parameters were performed using the Large-scale Atomic/Molecular Massively Parallel Simulator (LAMMPS).[34] We calculated the equilibrium lattice constants, elastic constants, and Birch–Murnaghan equation of state,[35,36] as described in Sec. S4. The pressure vs relative volume curve calculated using the Tersoff potential was in very good agreement with the experimental[21,22] and DFT data[21] up to 25 GPa, as shown in Fig. 1(c). In addition, the mechanical properties and lattice parameters calculated with MD were compared with the expected values obtained from DFT calculations, and a radar plot was created, as shown in Fig. 1(d). The perimeter of the radar plot corresponds to zero error, while the center point corresponds to 100% error. The optimized potential accurately predicted the lattice parameters of the crystal (a, b, and c), the elastic constants (C_{ij}), the bulk modulus K, and the Poisson ratio (v) of *ortho*-Mo_2C. The calculated properties are reported in Table II.

The new Tersoff potential was then demonstrated with simulations of indentation of *ortho*-Mo_2C. To create the model material, the primitive cell was replicated up to a size of ~16 nm in the directions perpendicular to the indentation and 11 nm in the direction of the load. Figure 2(a) shows the indentation model. Periodic boundary conditions were applied in the two directions perpendicular to the indentation. A free boundary was applied to the face in contact with the indenter. The structures were geometrically optimized and the temperature and pressure were equilibrated following the steps described in Sec. S4.

The simulation process followed the protocols for modeling indentation reported in the literature.[37] The atoms were divided into three regions. The positions of atoms in the bottommost atomic layers were fixed. Above that, several atomic layers of atoms were subject to the Langevin thermostat that maintained a constant temperature of 300 K using the canonical ensemble (NVT). The remainder of the atoms were unconstrained and free to deform under a microcanonical ensemble (NVE). The interactions of the indenter with the atoms were modeled using a repulsive force F that follows the equation $F(r) = k(R - r)^2$, where k is the force constant with a fixed value of 10 eV/Å^2, R is the indenter radius, and r is the distance

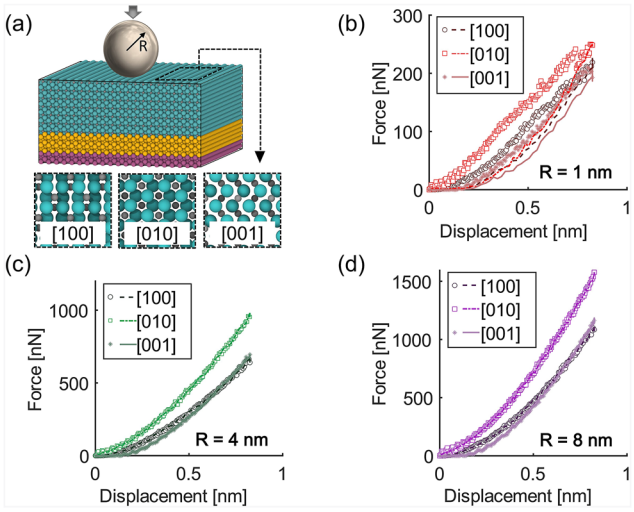

FIG. 2. (a) Schematic of the nanoindentation simulations where the atom color corresponds to the following: teal—unconstrained Mo, gray—unconstrained C, orange—thermostatted Mo and C, and magenta—fixed Mo and C. The virtual indenter is represented by a rigid sphere of radius R. Close-up images of the surface as viewed from the three different loading directions are shown below. Force vs displacement curves for (b) 1 nm, (c) 4 nm, and (d) 8 nm radius indenters. In (b), for each case, the loading data (symbols) are at a higher force than the unloading data (lines); in (c) and (d), the loading and unloading data overlap.

31 August 2023 09:13:32

© Author(s) 2023

from the *ortho*-Mo_2C atoms to the indenter center. Three different sized spherical indenters were modeled having radii of 1, 4, and 8 nm. To model indentation, the sphere was displaced toward the sample at a constant speed of 0.5 m/s in three different orientations relative to the crystallographic lattice—[100], [010], and [001]. The system was subjected to indentation loading for 1.6 ns, followed by a holding period at the maximum tip displacement of 0.8 nm below the original *ortho*-Mo_2C surface for 0.15 ns, and finally unloading at 0.5 m/s for 1.6 ns.

The force–displacement results for indentation with 1, 4, and 8 nm radius indenters loading in the [100], [010], and [001] directions are shown in Figs. 2(b)–2(d). Hysteresis between loading and unloading curves is observed only when the 1 nm radius indenter is used, indicating plastic deformation. This confirms that the force field can model the plastic response of the material, although it was trained only for elastic behavior. However, here, we are focused on elasticity and therefore subsequently analyzed only the behavior of *ortho*-Mo_2C in response to interactions with the 4 and 8 nm indenters. For the two larger indenters, there is a consistent effect of orientation, with the largest force response to indentation in the [010] direction. For the other two orientations, at small displacements ($\leqslant$0.5 nm), the force is slightly higher in [100], but, at larger displacements, the force is similar in [100] and [001].

The elastic constants calculated using the Tersoff potential and DFT are given in Table II. In bulk *ortho*-Mo_2C, the elastic constants C_{11}, C_{22}, and C_{33} should correspond to the [100], [010], and [001] loading directions. However, per Table S4, $C_{33} \approx C_{22} > C_{11}$, which is inconsistent with the indentation force in Fig. 2 that is highest for [010] and lowest (at least at low strain) for [001]. Therefore, the force response to indentation in the three different directions cannot be explained by the direction-dependent elastic constants. This is partially due to the fact that the compression caused by spherical indentation is not uniaxial.[38] In addition, the response to indentation at the nanoscale is affected by both surface accommodation and the local stress atomic behavior.

To understand the directional anisotropy of the indentation response, we analyzed the distributions of per-atom von Mises stress and strain, as well as the atom displacement vectors, at the maximum indentation depth with the 8 nm indenter, as shown in Fig. 3. The strain patterns shown in Fig. 3(a) are visually quite different for the three different orientations. For example, the high-strain regions (red color) extend furthest below the contact in the [010] case and appears to be most isolated near the contact for [100]. In addition, there are regions of localized high strain that reflect the lattice pattern in the [010] case. Additional information is provided by the displacement vectors in Fig. 3(b), which shows that the atoms moved predominantly in the direction of indentation for the [001] case. This indicates that, in [001], atoms are easier to compress and hydrostatic loading from the spherical tip plays a smaller role in the deformation than the other orientations. The most lateral movement is exhibited by atoms in response to loading in the [100] direction. In the [010] case, displacement is in the direction of the indentation below the center of the contact, and there is atom movement in the lateral direction only near the corners of the contact area. Compression in the [010] direction is accommodated by the layer-like distribution of the atoms in this orientation [see Fig. 2(a)]. Finally, the stress distributions shown in Fig. 3(c) qualitatively differ for the three different orientations.

The visual trends seen in Fig. 3(c) were quantified by analyzing the von Mises stress as a function of depth along the centerline of the contact and as a function of radial position at the maximum stress depth. The results for the 8 nm indenter are shown in Figs. 4(a) and 4(b). Generally, the shape of the stress profiles is consistent

31 August 2023 09:13:32

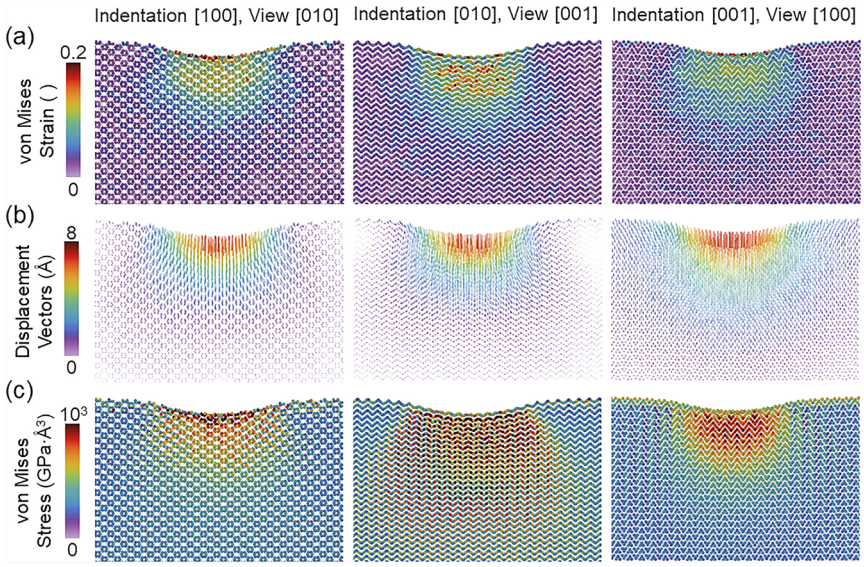

FIG. 3. Cross section snapshots of the *ortho*-Mo_2C simulation with the 8 nm indenter at an indenter displacement of 0.8 nm in the [100], [010], and [001] directions with atoms colored based on their (a) von Mises strain, (b) displacement vectors, and (c) von Mises stress.

© Author(s) 2023

with the approximation to the biaxial stress state predicted by continuum theory for a spherical indenter. For all loading directions, the maximum stress is just below and at the center of the contact. In addition, at the region of highest stress, the stress is largest for [010], consistent with the force-displacement trends in Fig. 2(d).

The most significant component of the von Mises stress is compression in the loading direction and, consistent with continuum theory, this stress is several times larger than the shear stress and the normal stresses in the two directions orthogonal to loading. However, closer analysis of the orthogonal stresses reveals an important difference between the response of the material to loading in different directions. In an ideal biaxial stress state, the stress in the two directions orthogonal to the loading direction is the same. However, due to the asymmetry of the *ortho*-Mo_2C structure, this is not observed in the simulations. The ratio of the normal virial stresses in the two non-loading directions is 1.4 for [100], 4.0 for [010], and 1.6 for [001]. For all three loading directions, there is some asymmetry, and this effect is most significant for loading in [010] where the stress in the [100] direction is several times larger than that in the [001] direction. This emphasizes that the elastic behavior of near-surface material differs from continuum predictions and is instead correlated with the local arrangement of atoms.[39]

The atomic configurations within the material, as viewed from the three loading directions are, even visually, quite different, as shown in Fig. 2(a). To understand how the atomic structure determines the direction-dependent force-displacement response of Mo_2C, we isolated the repeating unit load-bearing atom groups for each loading direction, as shown in Fig. 4(c). The ability of the repeating atom groups to resist deformation can be quantified in terms of the distance between neighboring atoms and the orientation of those atoms with respect to the direction of the load. Based on this concept, we calculated a resistance parameter R_m from the product of the distance and orientation of atom pairs (see supplementary material Sec. S5). A small value of R_m corresponds to short bonds that are highly aligned with the loading direction and, therefore, a large force response to displacement. This parameter was calculated to be 0.68 for loading in [010], 0.94 in [100], and 1.27 in [001]. The R_m for [010] is the smallest, consistent with the observation that the force response to indentation is largest in this direction in Figs. 2(b)–2(d). Similarly, R_m is slightly smaller for [100] than for [001], consistent with the higher force for [100] at small displacements. Although this parameter is only a rough approximation and does not capture the non-linear effect of distance on the force between atoms, it effectively quantifies the relationship between the atomic structure and the initial anisotropic force-displacement response of the material for different loading directions.

In summary, parameters for a Tersoff potential for molybdenum carbide were developed. The parameterization was able to accurately model the lattice constants, elastic mechanical properties, and the equation of state of *ortho*-Mo_2C. Classical MD models of indentation with different indenter radii using the new potential showed that *ortho*-Mo_2C is anisotropic. The *ortho*-Mo_2C model was stiffer in the [010] direction followed by the [100] and then [001]. The anisotropy was analyzed in terms of the distribution

31 August 2023 09:13:32

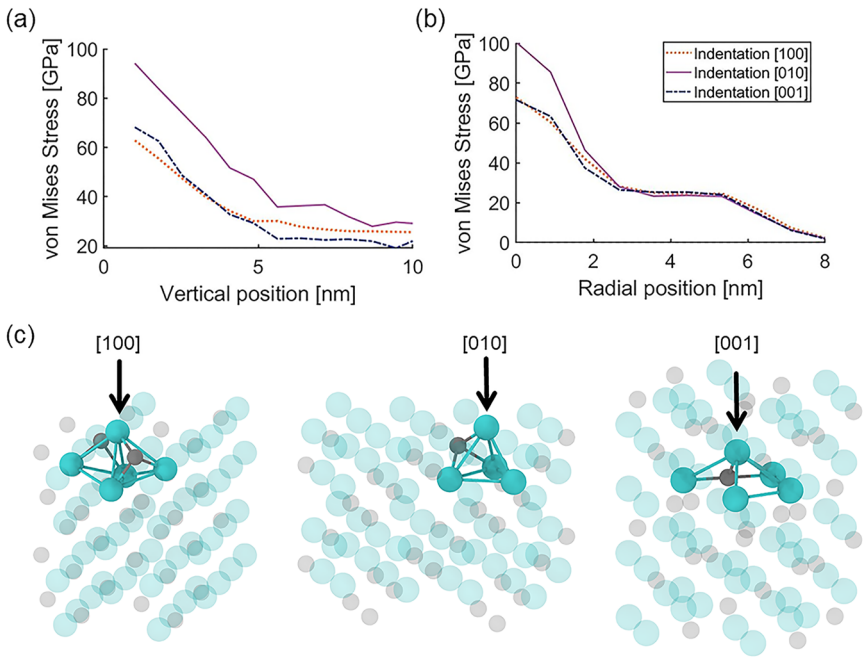

FIG. 4. Line profiles of the average von Mises stress with the 8 nm indenter at an indenter displacement of 0.8 nm (a) at the center of the contact as a function of depth below the surface and (b) at a depth of 0.35 nm below the original surface as a function of radial position. (c) Snapshots of the repeating unit load-bearing atom groups for loading in the [100], [010], and [001] directions. Atoms not in the repeating units are shown faded for context. The direction of load is identified by a black arrow.

© Author(s) 2023

of atomic stress and strain within the material and correlated with the alignment of the atoms with respect to the direction of indentation.

The supplementary material document contains an explanation of the naming convention for the Mo_2C structure, a summary of the Tersoff formalism and equations, the parameters for two alternate Tersoff potentials for *ortho*-Mo_2C, description of how the new parameter sets were evaluated in MD simulations, and details of the calculation of the resistance metric used to quantify bond distance and alignment with the loading direction.

This work was supported by Air Force Office of Scientific Research (AFOSR) Award Nos. FA9550-19-1-0035 and FA9550-19-1-7048. We also thank Abrar Faiyad for performing the resistance metric calculations.

AUTHOR DECLARATIONS

Conflict of Interest

The authors have no conflicts to disclose.

Author Contributions

I.M.P.E. and Y.K. contributed equally to this work.

Ingrid M. Padilla Espinosa: Formal analysis (equal); Investigation (equal); Writing – original draft (equal). **Yenal Karaaslan**: Formal analysis (equal); Investigation (equal); Writing – original draft (equal). **Cem Sevik**: Conceptualization (equal); Supervision (equal). **Ashlie Martini**: Conceptualization (equal); Supervision (equal); Writing – review and editing (equal).

DATA AVAILABILITY

The data that support the findings of this study, including the Tersoff force field parameters for *ortho*-Mo_2C, are available within the article and its supplementary material.

REFERENCES

[1]A. K. Kuleshov, V. V. Uglov, and D. P. Rusalsky, "Hard and wear-resistant niobium, molybdenum carbide layered coatings on WC-Co tools produced by ion bombardment and cathodic vacuum arc deposition," Surf. Coat. Technol. **395**, 125920 (2020).
[2]O. Rabi, E. Pervaiz, R. Zahra, M. Ali, and M. B. K. Niazi, "An inclusive review on the synthesis of molybdenum carbide and its hybrids as catalyst for electrochemical water splitting," Mol. Catal. **494**, 111116 (2020).
[3]S. Upadhyay and O. P. Pandey, "Review-synthesis and electrochemical applications of molybdenum carbide: Recent progress and perspectives," J. Electrochem. Soc. **169**, 016511 (2022).
[4]T. Ohmura, "Recent advances in indentation techniques and their application to mechanical characterization," Mater. Trans. **62**, 563–569 (2021).
[5]S. Breumier, A. Villani, C. Maurice, M. Lévesque, and G. Kermouche, "Effect of crystal orientation on indentation-induced residual stress field: Simulation and experimental validation," Mater. Des. **169**, 107659 (2019).
[6]B. Ernst, S. Keim, and U. Tetzlaff, "On the anisotropic indentation modulus and anisotropic creep behavior of β-Sn characterized by nanoindentation methods," Mater. Sci. Eng., A **848**, 143392 (2022).
[7]E. Amitay-Sadovsky, S. R. Cohen, and H. D. Wagner, "Nanoscale shear and indentation measurements in transcrystalline α-isotactic polypropylene," Macromolecules **34**, 1252–1257 (2001).
[8]S. Jiapeng, L. Cheng, J. Han, A. Ma, and L. Fang, "Nanoindentation induced deformation and pop-in events in a silicon crystal: Molecular dynamics simulation and experiment," Sci. Rep. **7**, 10282 (2017).
[9]M. Chen, A. M. Christmann, A. R. Muniz, A. Ramasubramaniam, and D. Maroudas, "Molecular-dynamics analysis of nanoindentation of graphene nanomeshes: Implications for 2D mechanical metamaterials," ACS Appl. Nano Mater. **3**, 3613–3624 (2020).
[10]A. P. Moore, C. Deo, M. I. Baskes, M. A. Okuniewski, and D. L. McDowell, "Understanding the uncertainty of interatomic potentials' parameters and formalism," Comput. Mater. Sci. **126**, 308–320 (2017).
[11]M. Nagai, H. Tominaga, and S. Omi, "CO adsorption on molybdenum carbides and molecular simulation," Langmuir **16**, 10215–10220 (2000).
[12]D. R. Pratt, L. S. Morrissey, and S. Nakhla, "Molecular dynamics simulations of nanoindentation—The importance of force field choice on the predicted elastic modulus of FCC aluminum," Mol. Simul. **46**, 923–931 (2020).
[13]S. M. Handrigan, L. S. Morrissey, and S. Nakhla, "Investigating various many-body force fields for their ability to predict reduction in elastic modulus due to vacancies using molecular dynamics simulations," Mol. Simul. **45**, 1341–1352 (2019).
[14]A. V. Redkov, A. V. Osipov, and S. A. Kukushkin, "Molecular dynamics simulation of the indentation of nanoscale films on a substrate," Tech. Phys. Lett. **42**, 639–643 (2016).
[15]Y. Zhao, X. Peng, T. Fu, C. Huang, C. Feng, D. Yin, and Z. Wang, "Molecular dynamics simulation of nano-indentation of (111) cubic boron nitride with optimized Tersoff potential," Appl. Surf. Sci. **382**, 309–315 (2016).
[16]G. Rajasekaran, R. Kumar, and A. Parashar, "Tersoff potential with improved accuracy for simulating graphene in molecular dynamics environment," Mater. Res. Express **3**, 035011 (2016).
[17]S. Otani and Y. Ishizawa, "Preparation of Mo_2C single crystals by the floating zone method," J. Cryst. Growth **154**, 202–204 (1995).
[18]A. N. Christensen, "A neutron diffraction investigation on a crystal of alpha-Mo_2C," Acta Chem. Scand. **31a**, 509–511 (1977).
[19]J. R. dos Santos Politi, F. Viñes, J. A. Rodriguez, and F. Illas, "Atomic and electronic structure of molybdenum carbide phases: Bulk and low Miller-index surfaces," Phys. Chem. Chem. Phys. **15**, 12617 (2013).
[20]M. I. Naher and S. H. Naqib, "Possible applications of Mo_2C in the orthorhombic and hexagonal phases explored via ab-initio investigations of elastic, bonding, optoelectronic and thermophysical properties," Results Phys. **37**, 105505 (2022).
[21]H. Liang, R. He, L. Liu, W. Zhang, and L. Fang, "Investigating the elastic, mechanical, and thermal properties of polycrystalline Mo_2C under high pressure and high temperature," Ceram. Int. **49**, 7341 (2022).
[22]J. Haines, J. M. Léger, C. Chateau, and J. E. Lowther, "Experimental and theoretical investigation of Mo_2C at high pressure," J. Phys.: Condens. Matter **13**, 2447 (2001).
[23]Y. Karaaslan, H. Yapicioglu, and C. Sevik, "Assessment of thermal transport properties of group-III nitrides: A classical molecular dynamics study with transferable Tersoff-type interatomic potentials," Phys. Rev. Appl. **13**, 034027 (2020).
[24]Y. Karaaslan, H. Yapicioglu, and C. Sevik, "Optimizing the thermal transport properties of single layer (2D) transition metal dicalcogenides (TMD)," Eskişehir Tech. Univ. J. Sci. Technol., A **20**, 373–392 (2019).
[25]A. Kandemir, H. Yapicioglu, A. Kinaci, T. Çağın, and C. Sevik, "Thermal transport properties of MoS_2 and $MoSe_2$ monolayers," Nanotechnology **27**, 055703 (2016).
[26]J. D. Gale and A. L. Rohl, "The general utility lattice program (GULP)," Mol. Simul. **29**, 291–341 (2003).
[27]G. Kresse and J. Hafner, "*Ab initio* molecular dynamics for liquid metals," Phys. Rev. B **47**, 558(R) (1993).
[28]P. E. Blöchl, "Projector augmented-wave method," Phys. Rev. B **50**, 17953–17979 (1994).

31 August 2023 09:13:32

© Author(s) 2023

[29]G. Kresse and J. Furthmüller, "Efficient iterative schemes for *ab initio* total-energy calculations using a plane-wave basis set," Phys. Rev. B **54**, 11169–11186 (1996).
[30]J. P. Perdew, K. Burke, and M. Ernzerhof, "Generalized gradient approximation made simple," Phys. Rev. Lett. **77**, 3865–3868 (1996).
[31]G. Kresse and D. Joubert, "From ultrasoft pseudopotentials to the projector augmented-wave method," Phys. Rev. B **59**, 1758–1775 (1999).
[32]A. Togo and I. Tanaka, "First principles phonon calculations in materials science," Scr. Mater. **108**, 1–5 (2015).
[33]S. Baroni, S. de Gironcoli, A. Dal Corso, and P. Giannozzi, "Phonons and related crystal properties from density-functional perturbation theory," Rev. Mod. Phys. **73**, 515–562 (2001).
[34]A. P. Thompson, H. M. Aktulga, R. Berger, D. S. Bolintineanu, W. M. Brown, P. S. Crozier, P. J. in 't Veld, A. Kohlmeyer, S. G. Moore, T. D. Nguyen, R. Shan, M. J. Stevens, J. Tranchida, C. Trott, and S. J. Plimpton, "LAMMPS—A flexible simulation tool for particle-based materials modeling at the atomic, meso, and continuum scales," Comput. Phys. Commun. **271**, 108171 (2022).
[35]F. Birch, "Finite elastic strain of cubic crystals," Phys. Rev. **71**, 809–824 (1947).
[36]F. D. Murnaghan, "The compressibility of media under extreme pressures," Proc. Natl. Acad. Sci. U. S. A. **30**, 244–247 (1944).
[37]J. Han, Y. Song, W. Tang, C. Wang, L. Fang, H. Zhu, J. Zhao, and J. Sun, "Reveal the deformation mechanism of (110) silicon from cryogenic temperature to elevated temperature by molecular dynamics simulation," Nanomaterials **9**, 1632 (2019).
[38]K. L. Johnson, "The correlation of indentation experiments," J. Mech. Phys. Solids **18**, 115–126 (1970).
[39]I. M. Padilla Espinosa, T. D. B. Jacobs, and A. Martini, "Atomistic simulations of the elastic compression of platinum nanoparticles," Nanoscale Res. Lett. **17**, 96 (2022).

31 August 2023 09:13:32

© Author(s) 2023